Nuclear Engineering and Technology 53 (2021) 1676–1685

Contents lists available at ScienceDirect

Nuclear Engineering and Technology

journal homepage: www.elsevier.com/locate/net

Original Article

BOTANI: High-fidelity multiphysics model for boron chemistry in CRUD deposits

Seungjin Seo [a], Byunggi Park [b], Sung Joong Kim [c], Ho Cheol Shin [d], Seo Jeong Lee [d], Minho Lee [a], Sungyeol Choi [a, *]

[a] Department of Nuclear and Quantum Engineering, Korea Advanced Institute of Science and Technology, 291 Daehak-ro, Yuseong-gu, Daejeon, 34141, South Korea
[b] Department of Energy Environmental Engineering, Soonchunhyang University, Asan, Chungcheongnam-do, 31560, South Korea
[c] Department of Nuclear Engineering, Hanyang University, 222 Wangsimni-ro, Seongdong-gu, Seoul, 04763, South Korea
[d] Korea Hydro & Nuclear Power Corporation, 70, 1312-gil, Yuseong-daero, Yuseong-Gu, Daejeon, 34101, South Korea

ARTICLE INFO

Article history:
Received 3 August 2020
Received in revised form
29 September 2020
Accepted 4 November 2020
Available online 8 November 2020

Keywords:
Axial offset anomaly
CRUD
Boron hideout
Evaporation-driven concentration
Multiphysics

ABSTRACT

We develop a new high-fidelity multiphysics model to simulate boron chemistry in the porous Chalk River Unidentified Deposit (CRUD) deposits. Heat transfer, capillary flow, solute transport, and chemical reactions are fully coupled. The evaporation of coolant in the deposits is included in governing equations modified by the volume-averaged assumption of wick boiling. The axial offset anomaly (AOA) of the Seabrook nuclear power plant is simulated. The new model reasonably predicts the distributions of temperature, pressure, velocity, volumetric boiling heat density, and chemical concentrations. In the thicker CRUD regions, 60% of the total heat is removed by evaporative heat transfer, causing boron species accumulation. The new model successfully shows the quantitative effect of coolant evaporation on the local distributions of boron. The total amount of boron in the CRUD layer increases by a factor of 1.21 when an evaporation-driven increase of soluble and precipitated boron concentrations is reflected. In addition, the concentrations of $B(OH)_3$ and $LiBO_2$ are estimated according to various conditions such as different CRUD thickness and porosity. At the end of the cycle in the AOA case, the total mass of boron incorporated in CRUD deposits of a reference single fuel rod is estimated to be about 0.5 mg.

1. Introduction

Several nuclear power plants worldwide have experienced axial offset anomaly (AOA) which is the significant depression of neutron flux at the upper parts of the core [1,2]. Since this depression decreases the safety margin of the reactor core, it is necessary to reduce its power level down to 70%, causing significant economic losses [3]. It is known that the Chalk River unidentified deposit or corrosion-related unidentified deposit (CRUD) on the surfaces of fuel cladding can trigger the AOA in a nuclear reactor [3–5]. In pressurized water reactor (PWR), CRUD deposits grows up to 100 μm by the accumulation of corrosion products in the primary coolant circuit [3,6–8]. The CRUD layer contains chimney-like structures where coolant evaporation actively occurs, producing wick-boiling structures [9]. Boron hideout within CRUD deposits is a key phenomenon linking the relationship between CRUD deposition and neutron flux depression [10,11]. Unfortunately, it is still challenging to directlty observe the chemical nature of boron hideout under the operating conditions of nuclear reactor [3].

In order to improve understanding of boron chemistry, many previous studies tried to simulate the boron hideout within the CRUD layer during the operation of a nuclear power plant [9,12–21]. Some of them succeeded in predicting boron precipitation by using the mesoscale CRUD models. Other studies, such as Boron-induced Offset Anomaly (BOA) and MAMBA-3D, predict CRUD deposition and boron hideout for the entire core or the sub-assemblies, respectively [22–24]. In addition to these models, it is significant to expand our understanding of the roles of the coolant evaporation and the CRUD properties on local boron chemistry.

This study develops a new CRUD model to analyze boron chemistry in CRUD deposits. This model treats a single fuel rod as divided into four 2D planes facing sub-channels along the azimuthal direction. Multiphysics phenomena such as heat transfer, capillary flow, solute transport, and chemical reactions were fully

* Corresponding author.
E-mail address: sungyeolchoi@kaist.ac.kr (S. Choi).

https://doi.org/10.1016/j.net.2020.11.008

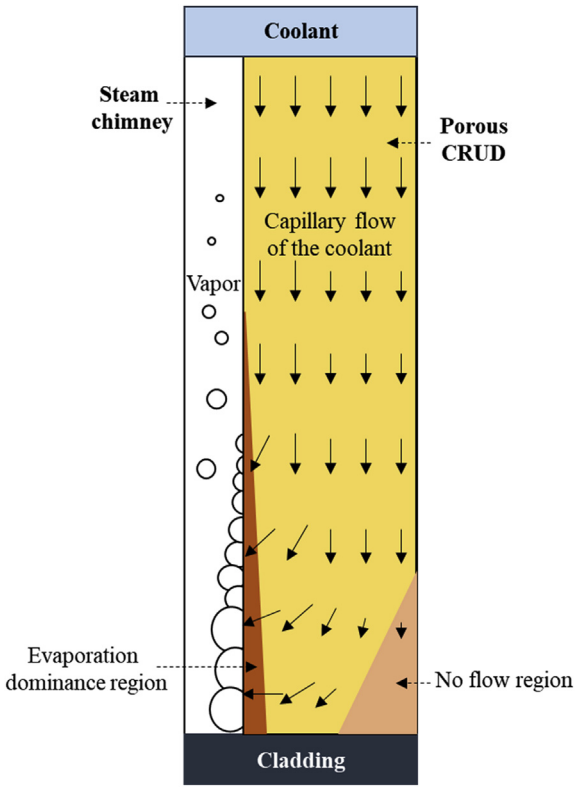

Fig. 1. Wick boiling structure within mesoscale CRUD layer, with internal flow of coolant and escaping flow of vapor.

coupled with the volume-averaged wick boiling assumption. As a reference case, the AOA of the Seabrook nuclear power plant was simulated. The new model successfully showed the quantitative effect of coolant evaporation on the distributions of boric acid and boron precipitations.

2. Methods

2.1. Multiphysics phenomena within CRUD deposits

During the operation of a nuclear power plant, the corrosion of metallic structural materials in the primary coolant system releases either soluble or particulate corrosion products such as Fe, Ni, Cr, Zr ions, ferrite, magnetite, chromium oxide, nickel oxide, nickel ferrite, and zirconium oxide. The corrosion products dissolved in the bulk coolant can be deposited on the upper spans of fuel assemblies by forming porous CRUD layers, from a few μm to over 100 μm [9,12]. While CRUD deposits grow, the evaporation of coolant within the deposits forms dense chimney-like structures, known as the wick boiling structure (Fig. 1).

Within CRUD deposits, thermal, fluid, mass transport, and chemical phenomena are closely related, as illustrated in Fig. 2. The sub-cooled nucleate boiling (SNB) in the wick boiling structure produces pressure drop, causing capillary coolant flow from the bulk coolant to the fuel surfaces. Higher mass evaporation rate leads to higher deposition rate of corrosion products, producing thicker CRUD deposits. In addition, soluble species including boric acid are transported together with coolant by capillary flow, and become locally concentrated in deposits. The different concentrations of chemical species not only promote diffusion but also stimulate chemical reactions towards equilibrium for reaction-

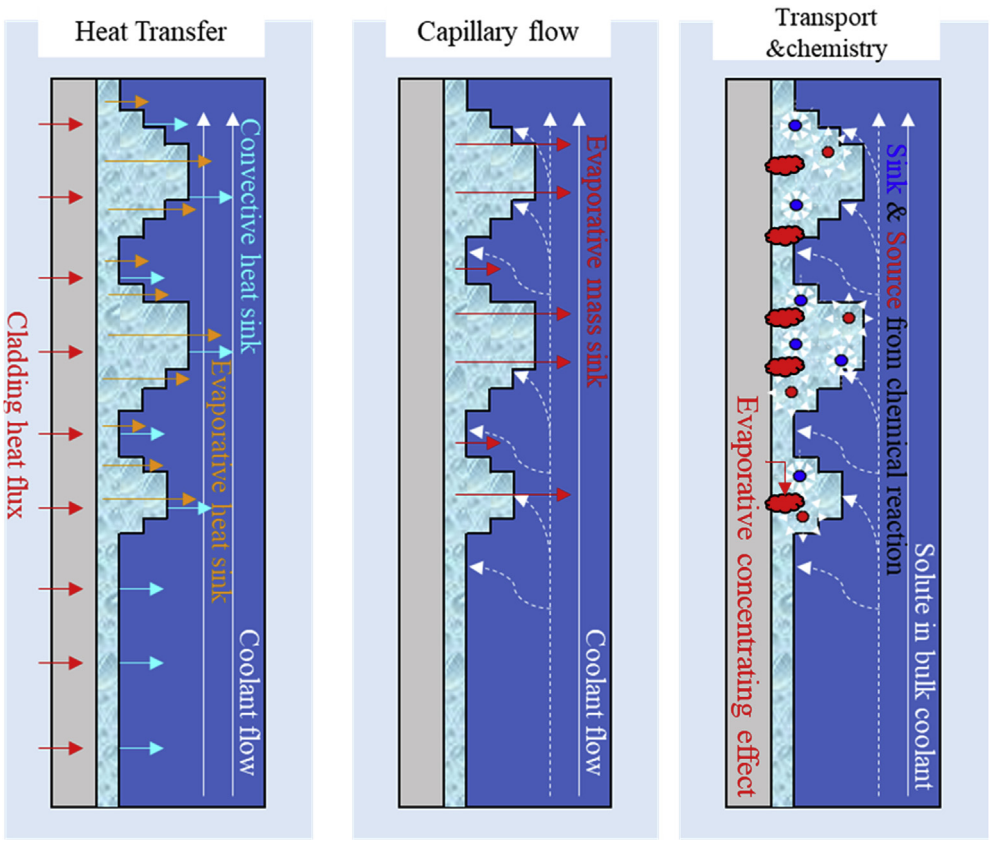

Fig. 2. Schematic of multi-physics within rod-scale CRUD layer through heat transfer, capillary flow, solute transport, and chemistry.

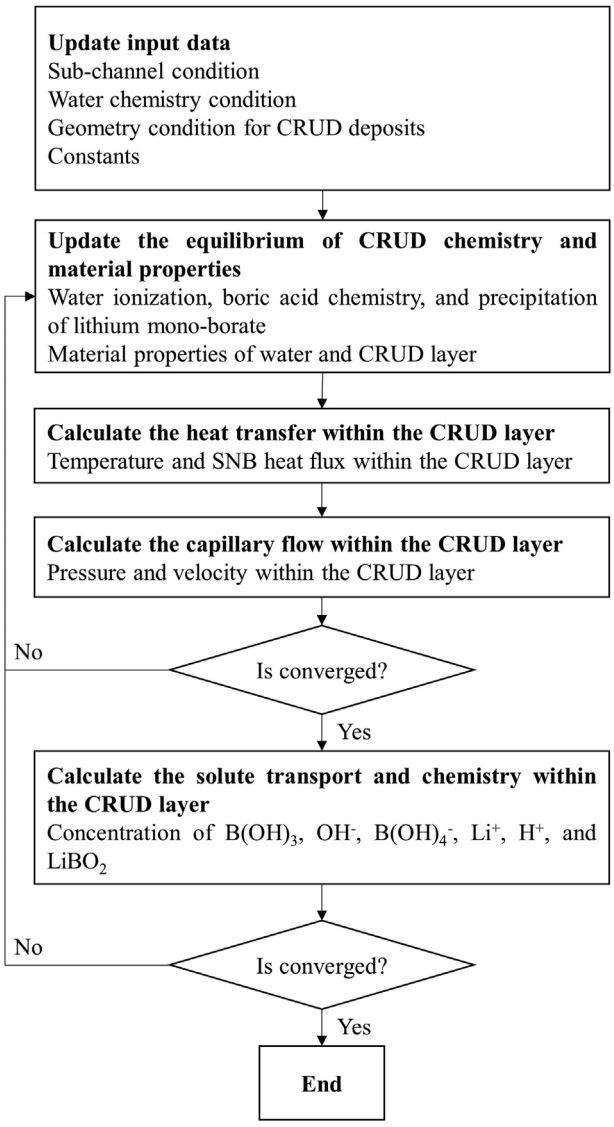

Fig. 3. A numerical algorithm for calculation of multi-physics within the CRUD layer.

convection-diffusion systems. Moreover, the saturation temperature of the coolant is a function of the concentration of soluble species such as boric acid. Importantly, the evaporation of coolant in CRUD deposits leads to the accumulation of boric acid. Most of the boric acid is not evaporated together with coolant. The evaporation-driven increase of boric acid concentration in CRUD deposits will also influence chemical reactions.

2.2. Heat transfer model

Based on the energy conservation, we derived the governing equation of steady-state heat transfer within porous CRUD deposits with an assumption of uniformly and densely distributed wick boiling chimney structures. Equation (1) incorporates conduction, convection, and SNB simultaneously. Equations (2) and (3) represent the entrance of heat from the cladding surface and its removal through the coolant interface.

$$\nabla\left(k_{th}^{eff}\nabla T\right)+\tau C_{v,w}\left(\frac{K}{\mu\varepsilon}\nabla P\right)\nabla T-\varepsilon q_{SNB}'''=0 \tag{1}$$

$$-k_{th}^{eff}\frac{\partial T}{\partial n}=q_{cladding} \tag{2}$$

$$-k_{th}^{eff}\frac{\partial T}{\partial n}=h_c(T-T_{Bulk}) \tag{3}$$

where k_{th}^{eff} is the effective thermal conductivity (W/mm·K); T is the temperature (K); P is the pressure (bar); τ is the tortuosity; μ is the viscosity of coolant (bar·s); κ is the permeability (mm^2); ε is the porosity; $C_{v,w}$ is the volumetric heat capacity of coolant (J/mm^3·K); q_{SNB}''' is the volumetric SNB heat density (W/mm^3); T_{Bulk} is the bulk coolant temperature (K); h_c is the convective heat transfer coefficient between CRUD and bulk coolant (W/mm^2·K); $q_{cladding}$ is the heat flux between CRUD and cladding (W/mm^2). All properties are defined in CRUD deposits except for T_{Bulk}, h_c, and $q_{cladding}$.

First, Equation (1) considers the heat conduction of mixtures of solid porous CRUD and liquid coolant by adopting effective thermal conductivity [25,26]. Second, the convective heat transfer is reflected in the governing equation by coupling it with Darcy's law for capillary flow within the porous medium. Third, the SNB heat

Table 1
Material properties of CRUD and coolant.

Material	Symbol	Description	Value range		Unit	Reference
CRUD	T	Temperature of the CRUD layer	560	630	K	–
	τ	Tortuosity of the CRUD layer	2.23		–	[17,32]
	ε	Porosity of the CRUD layer	0.8		–	[12]
	r_{chim}	Radius of steam chimney	2.5E-3		mm	[12]
	n_{chim}	Number density of the steam chimney	5000		#/mm^2	[12]
	λ	Pore diameter	2.5E-4	5.0E-4	μm	[17]
Coolant	T_{sat}	Saturation temperature	618.108	618.130	K	
	h_e	Evaporative heat transfer coefficient	1.93E-2	8.49E-2	W/(mm^{2}K)	[15]
	h_c	Convective heat transfer coefficient	2.5 E−2		W/(mm^{2}K)	[17,33]
	$C_{v,w}$	Volumetric heat capacity	1.62E-3	2.23E-3	J/(mm^{3}K)	[34]
	h_{fg}	Vaporization enthalpy	8.32E+1	9.74E+2	J/g	[35]
	ρ_w	Water density	5.41E-4	7.44E-4	g/mm^3	[36]
	ρ_v	Steam density	8.25E-5	1.29E-4	g/mm^3	[36]
	κ	Permeability	2.87E-9		mm^2	[17,32,37]
	μ	Viscosity	6.86E-10	9.19E-10	bar·s	[27]
	$D_{B(OH)_3}$	Diffusivity of the $B(OH)_3$ species	1.56E-2	2.10E-2	mm^2/s	[31]
	D_{OH^-}	Diffusivity of the OH^- species	9.13E-2	1.28E-1	mm^2/s	[31]
	$D_{B(OH)_4^-}$	Diffusivity of the $B(OH)_4^-$species	1.71E-2	2.31E-2	mm^2/s	[31]
	D_{Li^+}	Diffusivity of the Li^+ species	3.72E-2	4.15E-2	mm^2/s	[31]
	D_{H^+}	Diffusivity of the H^+ species	1.58E-1	2.21E-1	mm^2/s	[31]

Table 2
Thermal conductivity of CRUD.

Symbol	Description	Value range		Unit	Reference
k_{series}	Series thermal conductivity of the CRUD layer	5.24E-4	7.10E-4	W/(mm·K)	[17,37]
$k_{parallel}$	Parallel thermal conductivity of the CRUD layer	1.50E-3	1.53E-3	W/(mm·K)	[17,37]
k_f	Thermal conductivity of the fluid(coolant)	4.25E-4	5.78E-4	W/(mm·K)	[17,27]
$k_{s,Ni}$	Thermal conductivity of the Ni (v_f= 0)	6.45E-2	6.74E-2	W/(mm·K)	[17,28]
$k_{s,NiO}$	Thermal conductivity of the NiO (v_f= 0.15)	7.60E-3	8.51E-3	W/(mm·K)	[17,29]
$k_{s,NiFe_2O_4}$	Thermal conductivity of the $NiFe_2O_4$ (v_f= 0.75)	8E-3		W/(mm·K)	[17,30]
k_{s,Fe_3O_4}	Thermal conductivity of the Fe_3O_4 (v_f= 0.1)	3.37E-3	3.47E-3	W/(mm·K)	[17]
k_{s,ZrO_2}	Thermal conductivity of the ZrO_2 (v_f= 0)	1.96E-3	1.99E-3	W/(mm·K)	[17,29]

*v_f : volumetric fraction of component in the CRUD.

Table 3
Equilibrium and reaction rate constant of the chemical reactions. Chemical species concentrations were calculated from bulk boron and lithium concentration of Seabrook Unit 1 at the end of cycle 5.

Reaction	Chemical concentrations in coolant [mol/mm^3]		Reaction rate constant			Equilibrium constant		Reference
$H_2O \leftrightarrow H^+ + OH^-$	H^+	4.17E-14	k_f	7.86E-16	2.18E-14	3.34E-19	6.38E-18	[31,38,39]
	OH^-	2.94E-11	k_b	2.10E+9	3.00E+9			
$B(OH)_3 + OH^- \leftrightarrow B(OH)_4^-$	$B(OH)_3$	4.13823E-9	k_f	3.08E+4	3.30E+4	4.88E+1	6.94E+1	[25,31,40]
	OH^-	2.94E-11	k_b	4.76E+2	6.42E+2			
	$B(OH)_4^-$	2.57E-11						
$LiBO_2(s) + H_2O + H^+ \leftrightarrow Li^+ + B(OH)_3$	$LiBO_2$	1E-15	k_f	8.05E+4	1.64E+5	1.36E+7	2.75E+7	[25,31,41]
	H^+	4.17E-14						
	Li^+	8.11E-11	k_b	1.07E+1	1.46E+1			
	$B(OH)_3$	4.13823E-9						

*k_f: forward reaction rate constant; k_b: backward reaction rate constant.

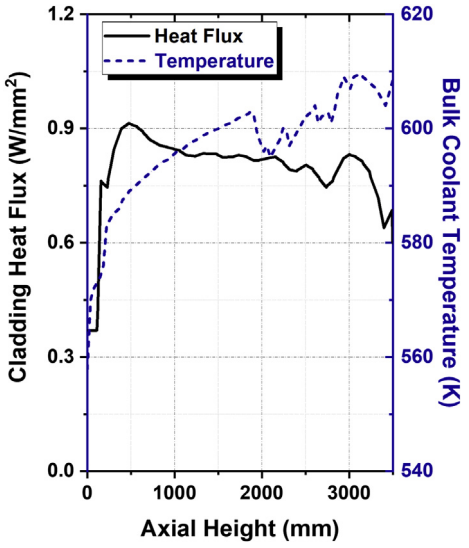

Fig. 4. Distribution of cladding heat flux and assumed bulk coolant temperature from Seabrook Unit 1 at the end of cycle 5. The geometry of the CRUD layer simulated by MAMBA-3D.

transfer is incorporated by the volume-averaged heat sink, q'''_{SNB}, determined by wick boiling mechanism.

The effective thermal conductivity was calculated by considering CRUD and coolant regions within porous deposits, along with their volume fractions and flow characteristics, as defined in Equation (4) [17]. Equations (5) and (6) present the series and parallel conductivities, respectively, along with the flow characteristics within the deposits. The thermal conductivity of coolant is calculated in Equation (7), and that of solid CRUD is obtained by the volume averaging of the thermal conductivity of its individual components as Equation (8) [17,27–30].

$$k_{CRUD} = \frac{1}{\frac{\xi}{k_{series}} + \frac{1-\xi}{k_{parallel}}} \tag{4}$$

$$k_{series} = \frac{1}{\frac{\varepsilon}{k_f} + \frac{1-\varepsilon}{k_s}} \tag{5}$$

$$k_{parallel} = \frac{\left(2 - D_f\right)\varepsilon\lambda_{max}^{D_\tau - 1}\left[1 - \left(\frac{\lambda_{min}}{\lambda_{max}}\right)^{D_\tau - D_f + 1}\right]}{t_{CRUD}^{D_\tau - 1}\left(D_\tau - D_f + 1\right)\left[1 - \left(\frac{\lambda_{min}}{\lambda_{max}}\right)^{2 - D_f}\right]}k_f + (1-\varepsilon)k_s \tag{6}$$

$$k_f = 0.686 + 7.3 * 10^{-10}P + 5.87*10^{-6}(T - 415)^2 \tag{7}$$

$$k_s = \prod_{i-1}^{n} k_{s,i}v_{f,i} \tag{8}$$

where D_f is the pore-free area dimension; D_τ is the tortuous capillarity dimension; t_{CRUD} is the thickness of CRUD (μm); ξ is the characteristic system length; $k_{s,i}$ is the thermal conductivity of the i-th solid component (W/mm·K); k_f is the thermal conductivity of coolant; $v_{f,i}$ is the volumetric fraction of the i-th solid component; λ_{max} and λ_{min} are the maximum and minimum pore diameters (μm).

In wick boiling, evaporation occurs at the surface of the steam chimney at μm scale. Since this small geometry presents challenges

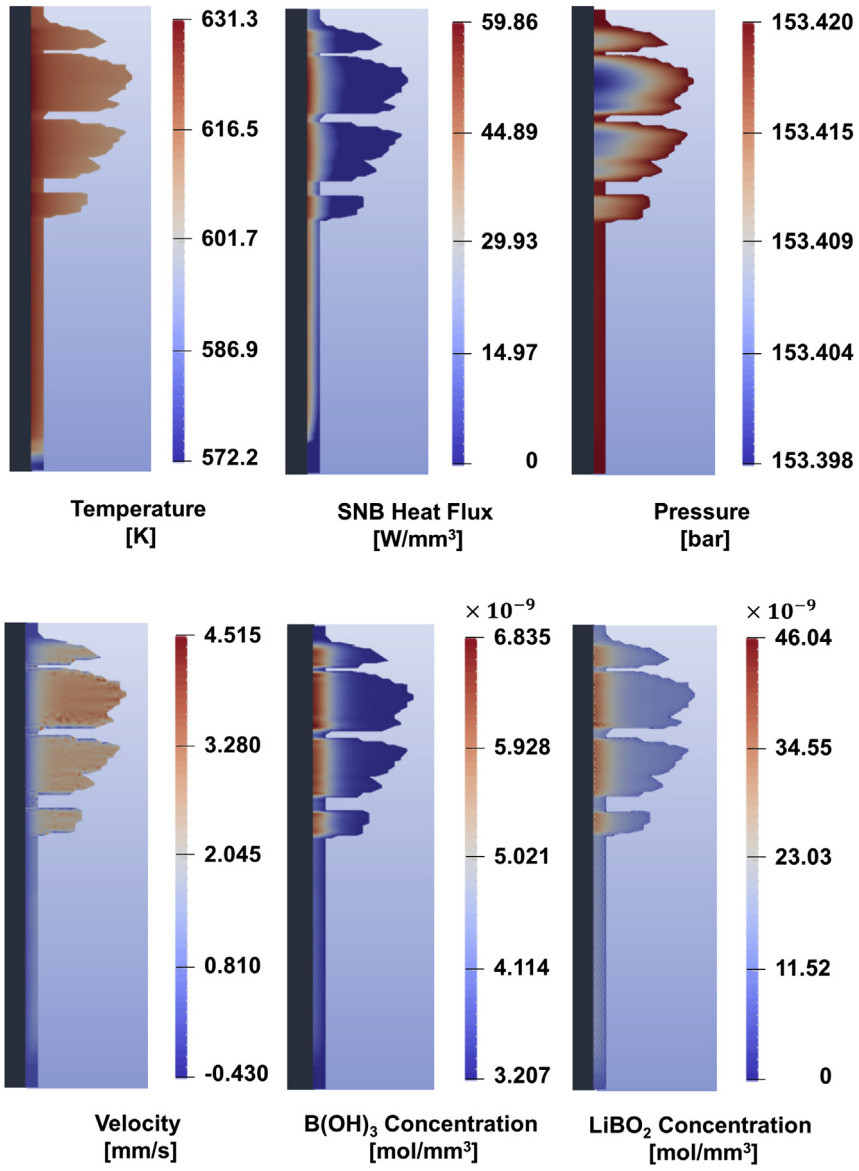

Fig. 5. Distribution of temperature, SNB heat flux, pressure, flow velocity, $B(OH)_3$ concentration and $LiBO_2$ concentration within the CRUD layer.

for using it in the macro-scale simulations, this model used the volume-averaged method for determining the evaporative volumetric heat sink, q'''_{SNB}, as defined in Equation (9).

$$q'''_{SNB} = \frac{q''_{SNB} n_{chim} A_{cell}}{V_{cell}} = 2\pi r_{chim} n_{chim} h_e (T - T_{sat}) \tag{9}$$

where q''_{SNB} is the SNB heat flux on the surface of the steam chimney (W/mm^2); A_{cell} is the area of the cell of the steam chimney (mm^2); r_{chim} is the radius of the steam chimney (mm); n_{chim} is the number density of steam chimney (#/mm^2); h_e is the evaporative heat transfer coefficient of water in the wick boiling structure (W/mm^2·K); T_{sat} is the saturation temperature (K); V_{cell} is the volume of the cell (mm^3).

The saturation temperature of the coolant (T_{sat}) was calculated as the function of the concentration of soluble species, mostly boric acid, using Equations (10) and (11).

$$T_{sat} = 618.09 + 199.01(1 - a_w) - 952.74(1 - a_w)^2 + 26013.9(1 - a_w)^3 - 262916.0(1 - a_w)^4 + 997166.1(1 - a_w)^5 \tag{10}$$

$$a_w = \frac{m_w}{m_w + \sum_{all} m_i} \tag{11}$$

where a_w is the activity of coolant; m_i is molality of the i-th species (mol/kg); m_w is molaity of water molecules (mol/kg).

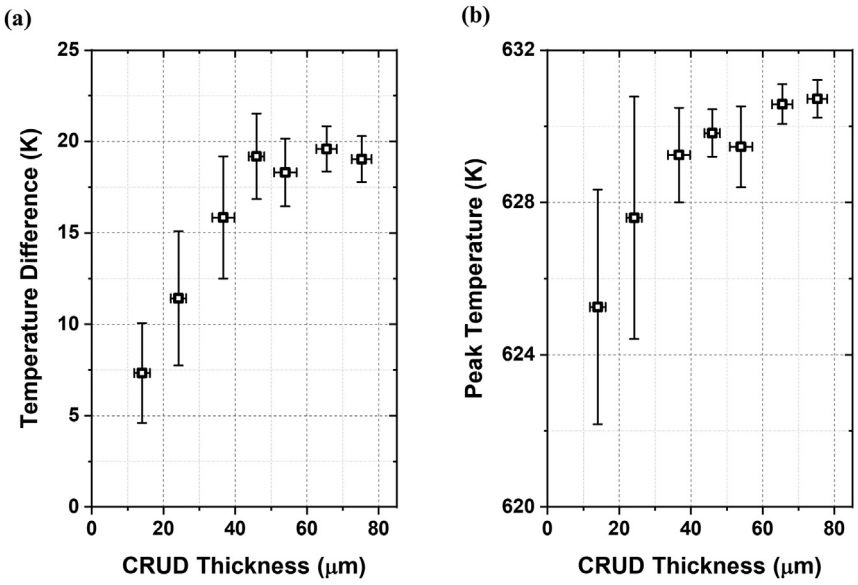

Fig. 6. (a) Distribution of radial temperature difference (between cladding interface and coolant interface) and (b) radial peak temperature (near cladding interface) along with CRUD thickness.

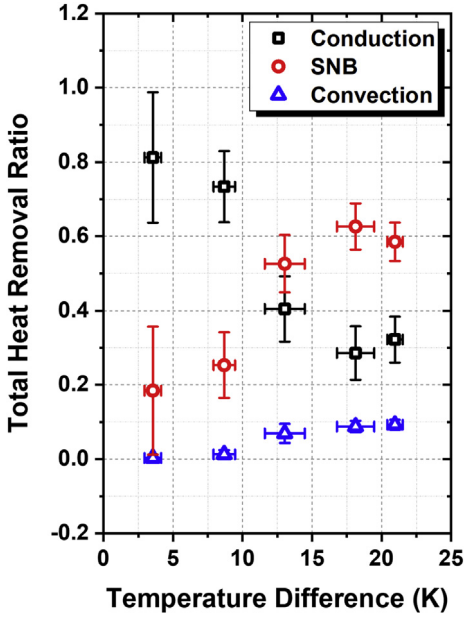

Fig. 7. The ratio of total heat removal across the CRUD layer in terms of conduction, convection, and evaporative heat sink.

Equation (12) gives the evaporative heat transfer coefficient of coolant on the surface of the steam chimney, as suggested by Pan et al. [12]. The convective heat transfer coefficient between CRUD and bulk coolant was set at 25,000 W/m^2·K under PWR conditions.

$$h_e = \frac{2A}{2-A}\left(\frac{M_{H_2O}}{2\pi R}\right)^{\frac{1}{2}} \frac{h_{fg}^2}{T^{3/2}\left(\overline{V}_w^v - \overline{V}_w^l\right)} \tag{12}$$

where A is the evaporation or condensation coefficient; R is the gas constant (J/mol·K); M_{H_2O} is the molecular weight of water (g/mol); h_{fg} is the vaporization enthalpy of water (J/g); $\overline{V}_w^v$ and $\overline{V}_w^l$ are the molecular of water and steam (m^3/mol).

2.3. Capillary flow model

Equation (13) presents the steady-state capillary flow equation derived from the mass conservation within CRUD deposits. The boundary condition of pressure is set as the pressure of bulk coolant at the coolant interface, as given in Equation (14). The capillary flow is driven by the evaporation of coolant, represented by the volume-averaged mass sink, when the coolant temperature is higher than its saturation temperature. Equation (15) provides the evaporative mass sink, m'''_{sink}, derived from the volume-averaged SNB heat density.

$$\nabla\left(-\rho_w \frac{K}{\mu}\nabla P\right) + \varepsilon m'''_{sink} = 0 \tag{13}$$

$$P = P_{coolant} \tag{14}$$

$$m'''_{sink} = \frac{q''_{SNB} n_{chim} A_{cell}}{V_{cell}\, h_{fg}} = \frac{2\pi r_{chim} n_{chim} h_e (T - T_{sat})}{h_{fg}} \tag{15}$$

where q''_{SNB} is the total SNB heat of the cell (W/mm^2); h_{fg} is the vaporization enthalpy of water (J/g); $P_{coolant}$ is the pressure of bulk coolant (bar).

2.4. Solute transport and chemistry model

By using Darcy's law, Equation (16) comprises terms representing diffusion, convection, chemical reaction, and evaporation-driven increase in soluble concentration. We used the immediate provision of the coolant species through the coolant interface, as defined in Equation (17). This model considers three chemical reactions, including the water ionization, the reaction of boric acid to $B(OH)_4^-$, and the precipitation of lithium monoborate, $LiBO_2$. We assumed that lithium hydroxide directly dissociated into lithium and hydroxyl ions. The chemical kinetics, RR_j, determine the generation and consumption rates of boron species during transport through diffusion and convection. The reaction of boric acid to convert $B(OH)_4^-$ has the most dominant reaction rate among the formation reactions of $B(OH)_4^-$, $B_2O(OH)_5^-$, $B_3O_3(OH)_4^-$, and

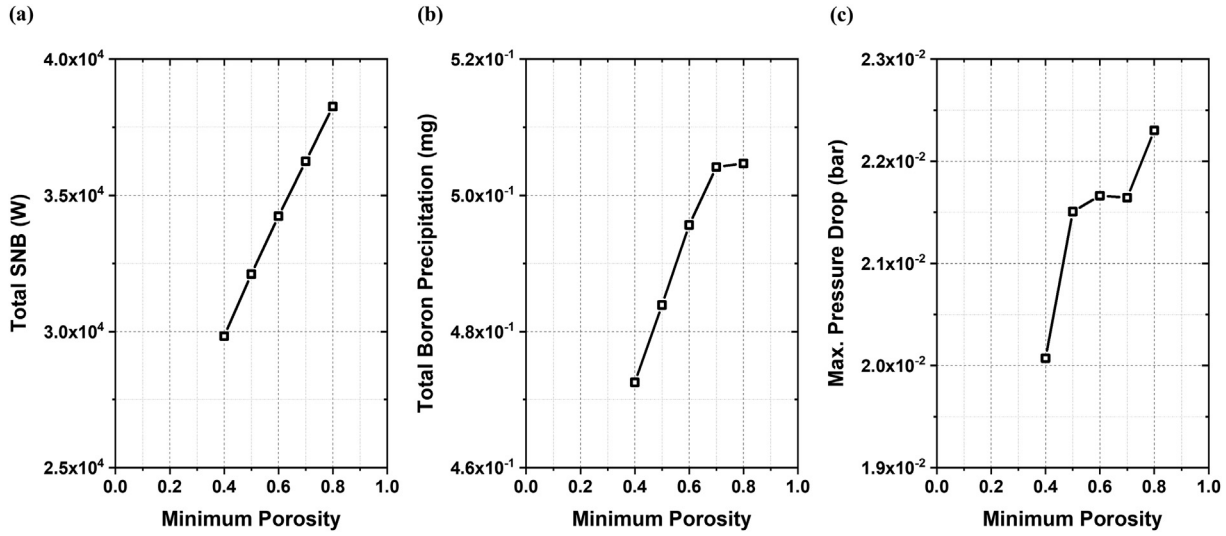

Fig. 8. (a) Change of the total amount of SNB, (b) boron precipitation, and (c) the maximum value of pressure drop within the CRUD layer along with porosity.

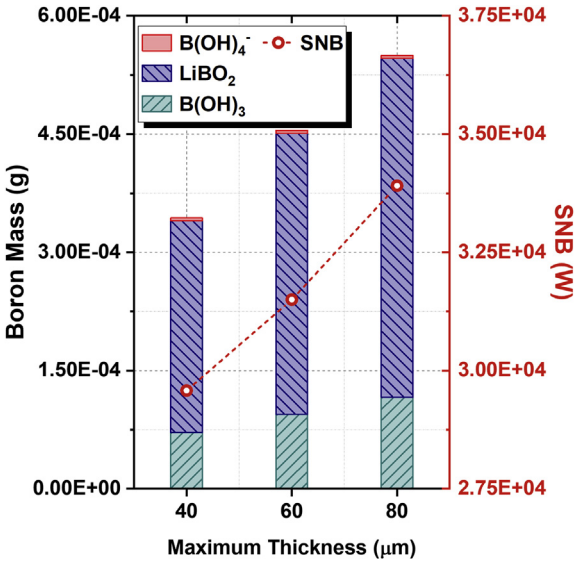

Fig. 9. Change of total amount of SNB heat removal and amount of boron depending on the CRUD layer thickness.

$B_3O_3(OH)_3$. The evaporation of coolant increases the local concentration of species at the evaporation sites, coupled with the volumetric SNB heat density.

$$\nabla(D_i\nabla C_i) + \nabla\left(\tau\frac{K}{\mu\varepsilon}\nabla PC_i\right) - \sum RR_j + \varepsilon\frac{2\pi r_c n_c h_e(T-T_s)}{h_{fg}\rho_w}C_i = 0 \tag{16}$$

$$C_i = C_{coolant,i} \tag{17}$$

where D_i is the diffusivity of the i-th species (mm^2/s); C_i is the concentration of the i-th species (mol/mm^3); $C_{coolant,i}$ is the concentration of the i-th species within the bulk coolant (mol/mm^3); RR_j is the reaction rate of the j-th chemical reaction ($mol/mm^3 \cdot s$).

The equilibrium constant, as a function of temperature, determines the equilibrium compositions of the reactant and product species. The equilibrium composition of the species is expressed as a formulation of activities. The activity is composed of molality and activity coefficient. For the reaction $B(OH)_3 + OH^- \rightarrow B(OH)_4^-$, the equilibrium constant and rate constants are calculated through Equation (18); for reaction $H_2O \rightarrow H^+ + OH^-$, through Equation (19); for reaction $LiBO_2 + H^+ + H_2O \rightarrow B(OH)_3 + Li^+$, through Equation (20).

$$K = \frac{a_{B(OH)_4^-}}{a_{B(OH)_3}a_{OH^-}} = \frac{m_{B(OH)_4^-}}{m_{B(OH)_3}m_{OH^-}}\frac{1}{\gamma_{OH^-}} = \frac{k_f}{k_b}\frac{\rho_w}{\gamma_{OH^-}} \tag{18}$$

$$K = \frac{a_{H^+}a_{OH^-}}{a_w} = \frac{m_{H^+}m_{OH^-}}{a_w}\gamma_{H^+}\gamma_{OH^-} = \frac{k_f}{k_b}\frac{\gamma_{H^+}\gamma_{OH^-}}{\rho_w^2} \tag{19}$$

$$K = \frac{a_{B(OH)_3}a_{Li^+}}{a_{LiBO_2}a_{H^+}a_w} = \frac{m_{B(OH)_3}m_{Li^+}}{m_{LiBO_2}m_{H^+}a_w}\frac{\gamma_{B(OH)_3}\gamma_{Li^+}}{\gamma_{LiBO_2}\gamma_{H^+}} = \frac{k_f}{k_b}\frac{1}{a_w}\frac{\gamma_{B(OH)_3}\gamma_{Li^+}}{\gamma_{LiBO_2}\gamma_{H^+}} \tag{20}$$

where a_i is the activity of the i-th species; m_i is molality of the i-th species (mol/kg); γ_i is the activity coefficient of the i-th species; ρ_w is density of the water (kg/m^3); k_b and k_f are backward and forward reaction rate constant.

2.5. Numerical approach and modeling conditions

The multiphysics model, written in the C++ language environment, is built on two open and numerical libraries: the Portable, Extensible Toolkit for Scientific Computation (PETSc), and libMesh. PETSc solves partial differential equations involving linear and nonlinear algebraic systems, allowing parallel computing based on the message passing interface (MPI). libMesh is a finite element method (FEM) library that supports arbitrary unstructured discretizations and adaptive mesh refinement. Gmsh is used as a finite element mesh generator. The mesh was generated along with CRUD deposits with a 10 μm seed-layer on the surface of the cladding. As a semi-3D model, a single fuel rod is divided into four parts facing sub-channels along the azimuthal direction. For the parallel calculations, we set a quarter of the fuel rod with one part having a sub-channel as the basic calculation unit.

Fig. 3 shows the calculation process of the multiphysics modeling. After initializing input parameters, temperature and volumetric SNB heat density in CRUD deposits are calculated by

using the heat transfer model at the steady-state. The evaporation-driven pressure and flow velocity distributions are obtained by using the capillary flow model at the steady-state. Because convective and evaporative heat transfers are coupled with the capillary flow, inner iterations between heat transfer and capillary flow are necessary. Based on the calculated temperature and velocity distributions, the solute transport and chemistry models calculate the concentrations of soluble and precipitated species. Outer iterations involving heat transfer, capillary flow, and solute transport are required to obtain the fully converged temperature, pressure, and concentration distributions.

Tables 1–3 list the values of parameters and reaction constants used in the modeling. The material properties and reaction parameters used in the model are functions of temperature.

3. Simulation case

In December 1995, Cycle 5 of Unit 1 in the Seabrook plant was designed to run for a longer duration at a higher power density. During the cycle, five fuel rods failed in assemblies G63 (rod K12), G64 (rod E12), G69 (rod M14), and G70 (rod G9 and L7) [25]. The maximum AOA observed during the cycle was approximately 3.3% at 260 effective full power day (EFPD) during the cycle. After shutdown, a thick CRUD layer was observed along the axial direction of the fuel assemblies. This AOA case at the end of the cycle was also simulated by MAMBA-3D [23]. Note that the axial power distribution of this simulation case is significantly changed. The heat flux in the low part of the fuel rod is much higher than that of the normal case.

We adopted the geometry of the thick CRUD deposits on a single fuel rod in the Seabrook plant from the previous study. Fig. 4 shows the cladding heat flux, bulk coolant temperature, and CRUD thickness along the axial direction of the fuel rod. For setting boundary conditions, the model used the sub-channel data of the Seabrook nuclear power plant given elsewhere [25].

4. Results

As shown in Fig. 5, thicker CRUD deposits resulted in higher temperature, reaching a maximum temperature of 631.30 K near the cladding surface. The temperature differences along the radial direction ranged from 10 to 20 K in CRUD deposits at the upper spans. The distributions of SNB heat density and pressure shows evaporation-driven capillary flow. The peak SNB heat density was 59.86 W/mm^3, occurring near the cladding interface at the thickest CRUD layer formed. At the same position, the maximum pressure drop of 0.02 bar occurred, which provided the capillary flow of approximately 4.52 mm/s that travels 100 μm in 0.022 s. The evaporative heat removal, 33,302 W, accounts for 40.17% of the total heat of a fuel rod, 82,907 W.

The concentrations of boron species, $B(OH)_3$ and $LiBO_2$, in the CRUD layer were positively correlated with CRUD thickness of and SNB heat density. The high concentration of $B(OH)_3$ was observed near the cladding surface at thick CRUD deposits, which was resulted from evaporation-driven concentrated species and capillary coolant flow. The accumulation of $B(OH)_3$ reached equilibrium when these two phenomena were balanced with the diffusion of boron. The concentrated $B(OH)_3$ increased the precipitation of $LiBO_2$ having retrograde solubility at reactor conditions. At the end of the cycle of the AOA case, the total mass of boron incorporated in CRUD deposits of a reference single fuel rod is estimated to be 57 mg. EPRI suggested that the 0.27 kg of boron hideout for the entire core during a cycle will lead to an axial offset of about −3%, with the maximum amount of boron hideout as the threshold of the AOA is 1.1 kg [3].

In the seed layer of CRUD for numerical simulation at the lower spans of the fuel rod, there were relatively low SNB heat density, slow capillary flow, low pressure drop, and low $B(OH)_3$ concentration. Unlike the normal operation of the nuclear reactor, the results showed small but still not negligible SNB heat density even at the lower part of the fuel rod because of the power shift in the case of the AOA.

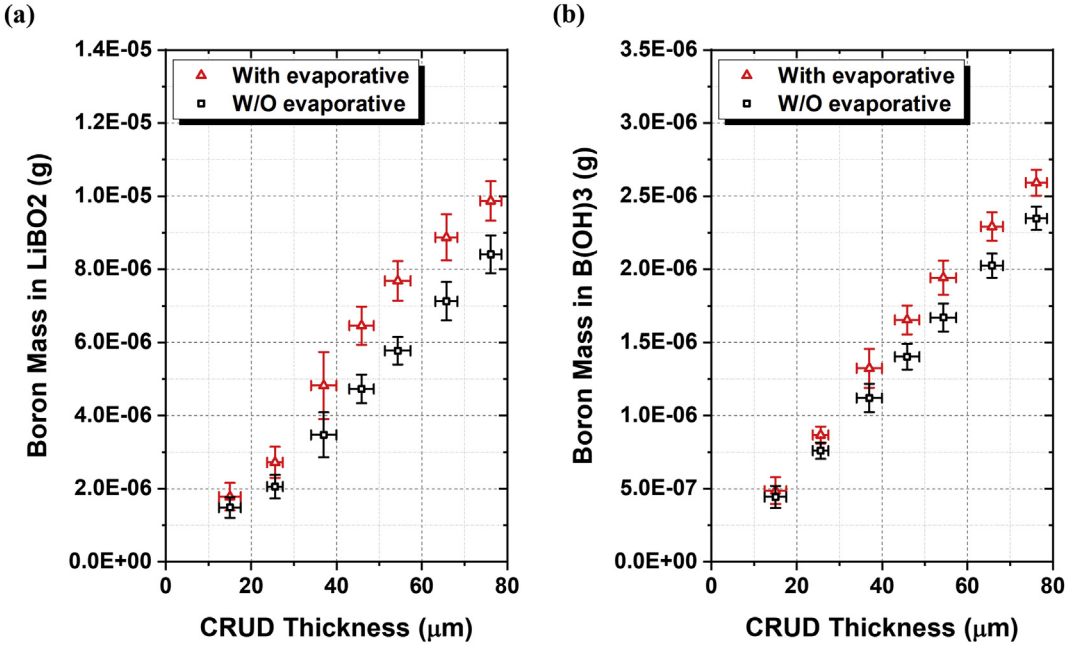

Fig. 10. Amount of boron mass in (a) $LiBO_2$ and (b) $B(OH)_3$ for each axial cell along with the thickness with and without the evaporative concentrating of the soluble species.

5. Discussion

5.1. Contribution of conduction, convection, and boiling for heat transfer

Fig. 6 plots the radial temperature difference and the peak temperature across the CRUD deposits according to the CRUD thickness. Due to the complicated structures of the deposits, there are multiple locations having the sample thickness. In the thick CRUD region, substantial contributions from the SNB heat sink cause reduction of the increasing rate of the radial temperature difference and peak temperature. According to the temperature difference, Fig. 7 shows the contribution of conduction, convection, and boiling for heat removal in CRUD deposits. SNB occurred when the coolant temperature is higher than its saturation temperature. In the region where the radial temperature difference is low, the contribution of conduction is the most dominant one. As the temperature difference increases, the boiling heat transfer increases and reaches up to the removal of 60% total heat. The convective heat transfer increases with boiling causing capillary flow, but it is not effective for all of the regions. The limited contribution of convection found in this macro-scale model agrees well with the result in the earlier study of a mesoscale model [13,17].

5.2. Influence of porosity of CRUD deposits

A range of porosity of CRUD deposits has been reported. Also, it has possibility to vary along with the precipitation reactions of boron and metal ions [3,31]. While the reference case has uniformly distributed porosity, the other case has a varying distribution, from 0.4 to 0.7. The porosity was assumed to linearly decrease as it approaches to the coolant interface from the cladding interface. Fig. 8 shows that denser CRUD deposits produced the less amount of boron precipitation with smaller SNB. The amount of SNB showed an almost linear proportional relationship with porosity. Higher CRUD temperature was estimated for the higher porosity case. Higher porosity caused a decrease in conductive heat transfer. The amount of boron precipitation showed a similar relationship with porosity except for high porosities from 0.7 to 0.8, where the upturn dramatically decreases. The decrease in porosity is also related to the decrease in boron precipitation because the equilibrium constant of the chemical reaction is proportional to the temperature.

5.3. Boron accumulation according to CRUD thickness

The growth of CRUD deposits is still difficult to be measured and simulated, so there is necessarily large uncertainty in CRUD thickness. The influence of CRUD thickness was quantified. Three different cases of end-of-cycle CRUD distribution were compared with maximum thicknesses of 40, 60, and 80 μm. The thickness of other CRUD regions was proportionally reduced. The same values or correlations were applied to all other conditions. Fig. 9 shows the total amount of boron and its chemical components as well as heat removal by SNB for the three cases. The total amount of boron within the CRUD is proportional to the CRUD thickness. The increase of solid boron is dominant comparing to that of the soluble boron species within the CRUD region. Total heat removal also increases when CRUD thickness increases, due to an increase of temperature difference across the CRUD layer.

5.4. Evaporation-driven increase of local boron concentrations

We calculated the effects of evaporation on the concentrations of soluble and precipitated boron in CRUD deposits by having and removing the last-term of Equation (16). Without evaporation-driven increase of boron concentrations, the accumulation of boron is driven by capillary flow from the bulk coolant. As shown in Fig. 10, the evaporation of coolant played significant roles to accumulate not only soluble $B(OH)_3$ but also precipitated $LiBO_2$. The concentration profile of $B(OH)_3$ was significantly changed from the almost uniform distribution to the one in proportion to the boiling. The uniform distribution showed that the capillary flow velocity was easily canceled out by the backward diffusional transport along the radial direction. The increased $B(OH)_3$ concentration intensified the precipitation of $LiBO_2$. The influence of evaporation on the concentration of $LiBO_2$ is more significant in the upper regions where evaporation is vigorous. As a result, the total amount of boron in the CRUD layer of the reference single fuel rod increased by a factor of 1.21.

5.5. Boron concentrations with and without CRUD deposits

Fig. 11 shows an increase in the amount of total boron along the axial direction. Total boron includes the ones is dissolved in the sub-channel coolant as well as the ones incorporated in the mixture of solid deposits and coolant in the CRUD layer. Comparing to the hypothetical case of no CRUD deposits, over 12% of more boron can be accumulated at the same height. All of the increased boron mass is concentrated in the deposits right next to the cladding surfaces.

6. Conclusions

The high-fidelity multiphysics FEM model, built on PETSc and libMesh, was developed to simulate boron chemistry in porous CRUD deposits. Heat transfer, capillary flow, solute transport, and chemical reactions were fully coupled. In particular, the evaporation of coolant in the wick boiling structure was included in governing equations modified by the volume-averaged assumption. The AOA case of the Seabrook nuclear power plant was simulated as the reference case. The new model reasonably predicted the distributions of temperature, pressure, velocity, volumetric SNB heat density, and chemical concentrations. The concentrations of $B(OH)_3$ and $LiBO_2$ were estimated according to various conditions such as

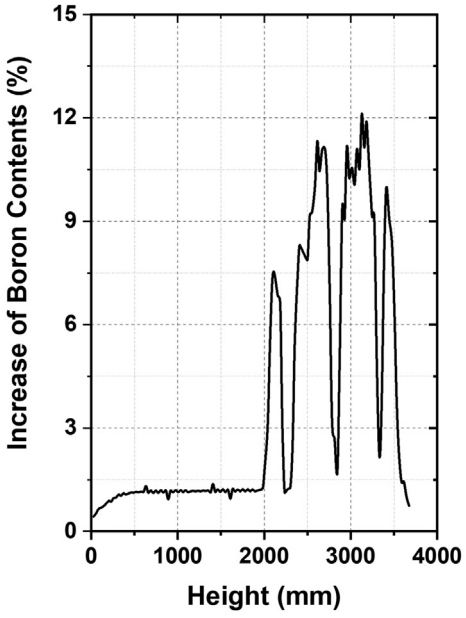

Fig. 11. Increase of boron contents when CRUD grows on the surface of the cladding and boron hideout occurs within the CRUD layer.

different CRUD thickness and porosity. The new model successfully showed the quantitative effect of coolant evaporation on the local distributions of boron. This model will be further improved by considering the growth of CRUD deposits, so that it will consider time-dependent calculations.

Declaration of competing interest

The authors declare that they have no known competing financial interests or personal relationships that could have appeared to influence the work reported in this paper.

Acknowledgements

This work was financially supported by Korea Hydro & Nuclear Power Co. Ltd. (Project No. L17S019000).

References

[1] P. Millet, E. Rapport, PWR Primary Water Chemistry Guidelines, vol. 1, EPRI, 1999. Rev. 4.
[2] A. Tigeras, J.L. Bretelle, E. Decossin, EDF AOA experience: chemical and thermal hydraulic analysis, in: Int. Conf. Water Chem. Nucl. React. Syst. Conf, San Fr, 2004, pp. 11–14.
[3] J. Deshon, PWR Axial Offset Anomaly (AOA) Guidelines, Revision 1, EPRI, Palo Alto, CA, 2004, p. 1008102.
[4] F.D. Nicholson, J. V Sarbutt, The effect of boiling on the mass transfer of corrosion products in high temperature, high pressure water circuits, Corrosion 36 (1980) 1–9.
[5] M. Zmitko, J. Kysela, J. Srank, T. Grygar, J. Subrt, Corrosion product deposits on cladding material, in: Water Chem. Corros. Control cladding Prim. Circuit components, IAEATECDOCS-1128, 1999, pp. 185–194.
[6] W.A. Byers, J. Deshon, Structure and chemistry of PWR crud, in: Int. Conf. Water Chem. Nucl. React. Syst. Conf. San Fr. USA, 2004, pp. 11–14.
[7] F. Franceschini, Andrew Godfrey, VERA Industry Applications, CASL Industry Council Meeting Charleston, South Carolina, 2017.
[8] W.A. Byers, J. Deshon, G.P. Gary, J.F. Small, J.B. Mcinvale, Crud metamorphosis at the Callaway plant, in: Proc. Inter. Conf. Water Chem. Nucl. React. Syst, 2006.
[9] P. Cohen, Heat and Mass Transfer for Boiling in Porous Deposits with Chimneys, 1974.
[10] A. Jaiswal, A Numerical Study on Parameters Affecting Boric Acid Transport and Chemistry within Fuel Corrosion Deposits during Crud Induced Power Shift, 2013.
[11] G. Sabol, J. Secker, J. Kormuth, H. Kunish, Rootcause Investigation of Axial Offset Anomalies, EPRI TR-108320, June, 1987.
[12] C. Pan, B.G. Jones, A.J. Machiels, Wick boiling performance in porous deposits with chimneys, in: AICHE/ANS Natl. Heat Transf. Conf. Symp. Multiph. Heat Transf. Denver, 1985.
[13] B.G. Park, S. Seo, S.J. Kim, J.H. Kim, S. Choi, Meso-scale multi-physics full coupling within porous CRUD deposits on nuclear fuel, J. Nucl. Mater. 512 (2018) 100–117.
[14] C. Pan, B.G. Jones, A.J. Machiels, Concentration levels of solutes in porous deposits with chimneys under wick boiling conditions, Nucl. Eng. Des. 99 (1987) 317–327.
[15] J. Henshaw, J.C. McGurk, H.E. Sims, A. Tuson, S. Dickinson, J. Deshon, A model of chemistry and thermal hydraulics in PWR fuel crud deposits, J. Nucl. Mater. 353 (2006) 1–11.
[16] I.U. Haq, Heat and Mass Transfer Analysis for Crud Coated PWR Fuel, 2011.
[17] M.P. Short, D. Hussey, B.K. Kendrick, T.M. Besmann, C.R. Stanek, S. Yip, Multiphysics modeling of porous CRUD deposits in nuclear reactors, J. Nucl. Mater. 443 (2013) 579–587.
[18] M. Jin, M. Short, Multiphysics modeling of two-phase film boiling within porous corrosion deposits, J. Comput. Phys. 316 (2016) 504–518.
[19] P.L. Frattini, J. Blok, S. Chauffriat, J. Sawick, J. Riddle, Axial offset anomaly: coupling PWR primary chemistry with core design, Nucl. Energy 40 (2001) 123–135.
[20] V.K. Dhir, Complete Numerical Simulation of Subcooled Flow Boiling in the Presence of Thermal and Chemical Interactions, Regents of the University of California, UCLA (US), 2003.
[21] B. Jones, Modeling and Thermal Performance Evaluation of Porous Crud Layers in Sub-cooled Boiling Region of Pwrs and Effects of Sub-cooled Nucleate Boiling on Anomalous Porous Crud Deposition on Fuel Pin Surfaces, University of Illinois at Urbana-Champaign (US), 2005.
[22] H.C. Shin, Solution for safety issue by using the code system for multi-physics reactor core engineering, in: Nuclear Safety & Security Information Conference 2018, Korea, (n.d).
[23] B. Kendrick, V. Petrov, D. Walker, A. Manera, CILC Studies with Comparative Analysis to Existing Plants, CASL-U-2013-0224-000, Los Alamos National Laboratory, 2013.
[24] B. Kendrick, C. Stanek, M. Short, MAMBA (MPO Advanced Model for Boron Analysis) Development for CASL: Update and Applications, 2014.
[25] D.J. Walter, A High Fidelity Multiphysics Framework for Modeling CRUD Deposition on PWR Fuel Rods, 2016.
[26] G. Wang, Improved Crud Heat Transfer Model for Dryout on Fuel Pin Surfaces at PWR Operating Conditions, 2009.
[27] P. Gierszewski, B. Mikic, N. Todreas, Property Correlations for Lithium, Sodium, Helium, FLiBe and Water in Fusion Reactor Applications (PFC-RR-80-12), Technical Report, Massachusetts Institute of Technology, Plasma Fusion Center, 1980.
[28] H. Watanabe, Thermal constants for Ni, NiO, MgO, MnO and CoO at low temperatures, Thermochim. Acta 218 (1993) 365–372.
[29] W.D. Kingery, J. Francl, R.L. Coble, T. Vasilos, Thermal conductivity: X, data for several pure oxide materials corrected to zero porosity, J. Am. Ceram. Soc. 37 (1954) 107–110.
[30] J. Mo/lgaard, W.W. Smeltzer, Thermal conductivity of magnetite and hematite, J. Appl. Phys. 42 (1971) 3644–3647.
[31] B.G. Park, I.H. Rhee, B.Y. Jung, K. Hong, Development of Water Chemistry Model in Crud Layer on Fuel Cladding, Korea Atomic Energy Research Institute, 2010.
[32] B. Yu, Analysis of flow in fractal porous media, Appl. Mech. Rev. 61 (2008).
[33] N.E. Todreas, M. Kazimi, Nuclear Systems Volume I: Thermal Hydraulic Fundamentals, CRC press, 2011.
[34] E.W. Lemmon, Thermophysical Properties of Fluid Systems, NIST Chem. Webb., 1998.
[35] S. Dickinson, J. Henshaw, J. McGurk, H. Sims, Modeling PWR Fuel Corrosion Product Deposition and Growth Processes: Final Report, EPRI, Palo Alto, CA, 2005, p. 1011743.
[36] J.H. Keenan, F.G. Keyes, Thermodynamic Properties of Steam, John Wiley and Sons, NewVork, Ny, 1963.
[37] Y. Shi, J. Xiao, S. Quan, M. Pan, R. Yuan, Fractal model for prediction of effective thermal conductivity of gas diffusion layer in proton exchange membrane fuel cell, J. Power Sources 185 (2008) 241–247.
[38] W.L. Marshall, E.U. Franck, Ion product of water substance, 0–1000 C, 1–10,000 bars New International Formulation and its background, J. Phys. Chem. Ref. Data 10 (1981) 295–304.
[39] J.H. Alexander, L. Luu, MULTEQ: Equilibrium of an Electrolytic Solution with Vapor-Liquid Partitioning and Precipitation: Volume 1, vol. 1, 1989. User's manual, Revision.
[40] O. Weres, Vapor pressure, speciation, and chemical activities in highly concentrated sodium borate solutions at 277 and 317° C, J. Solut. Chem. 24 (1995) 409–438.
[41] W.A. Byers, W.T. Lindsay, R.H. Kunig, Solubility of lithium monoborate in high-temperature water, J. Solut. Chem. 29 (2000) 541–559.